Applied Physics A (2025) 131:911
https://doi.org/10.1007/s00339-025-08977-y

Applied Physics A
Materials Science & Processing

S.I. : NOVEL AND ADVANCED MATERIALS FOR ENERGY AND BIOMEDICAL APPLICATIONS (INEEBA-2024)

3D $MnNi_2S_4$-MOF-67/rGO composite: a high-performance material for advanced supercapacitor applications

S. Antony Sakthi[1] · C. Mani[2] · K. Priyadarshini[3] · A. Niresha Gnana Mary[1] · E. Shinyjoy[4]

Received: 28 January 2025 / Accepted: 19 September 2025

Abstract

Improving the performance of metal-organic framework (MOF)-based electrode materials remains a significant challenge due to their inherent instability and poor electrical conductivity. In this study, we report the development of a novel $MnNi_2S_4$-MOF-67 composite, incorporating graphene oxide (GO) and ZIF-67 as both a structural template and precursor. The synergistic effect of GO and ZIF-67 enhances the specific surface area, introduces abundant active sites for redox reactions, and shortens ion diffusion pathways. As a result, the $MnNi_2S_4$-MOF-67 composite exhibits outstanding electrochemical performance, delivering a remarkable specific capacitance of 1940 F g^{-1} at 1 A g^{-1}. Furthermore, the material demonstrates excellent cycling stability, retaining 91% of its initial capacitance after 10,000 charge-discharge cycles at 5 A g^{-1}. When assembled into an asymmetric supercapacitor (ASC) with $MnNi_2S_4$-MOF-67@rGO//GO electrodes, the device achieves an impressive energy density of 45.90 Wh kg^{-1} at a power density of 1689 W kg^{-1}. These results highlight the potential of hybrid-structured electrodes in advancing next-generation high-energy-density asymmetric supercapacitors.

Keywords Supercapacitor electrode · $MnNi_2S_4$-MOF-67 · Reduced graphene oxide (rGO) · Energy storage and electrochemical stability

1 Introduction

The rapid advancement of energy storage technologies has spurred the development of high-performance supercapacitors to meet the growing demand for efficient and sustainable power sources [1–3]. Supercapacitors offer advantages such as high-power density, fast charge-discharge rates, and long cycle life over traditional batteries, making them ideal for applications ranging from portable electronics to electric vehicles [1, 4, 5]. However, limitations in energy density and cyclic stability remain challenges. To overcome these, we propose a novel electrode comprising a 3D $MnNi_2S_4$-MOF-67 framework anchored on reduced graphene oxide (rGO), combining the high surface area and porosity of $MnNi_2S_4$-MOF-67 with the excellent conductivity and mechanical support of rGO. This composite design enhances electrochemical properties, including specific capacitance, energy density, and cycle stability [6].

Transition metal sulfides like $MnNi_2S_4$ are attractive for energy storage due to their high conductivity and rich redox chemistry. With multiple oxidation states, $MnNi_2S_4$ facilitates faradaic reactions and delivers excellent theoretical capacitance. Studies confirm its notable electrochemical performance in supercapacitors, attributed to its high surface area and fast electron transport [1, 7–10]. Nonetheless, structural degradation during cycling necessitates composite strategies to improve stability [6, 11].

Metal-organic frameworks (MOFs), especially MOF-67 (cobalt-based), offer high surface area and tunable porosity, supporting applications in catalysis, gas storage, and electrochemical devices. In supercapacitors, MOF-67 provides ion transport pathways and accessible charge storage surfaces

✉ S. Antony Sakthi
santonysakthi@gmail.com

1 Department of Chemistry, St. Joseph's College, (Autonomous), Affiliated to Bharathidasan University, Tiruchirappalli 620 002, Tamil Nadu, India

2 Dr. C. Mani L A B S, Center for Green Energy, Tiruchirappalli 621 112, India

3 Department of Electronics and Communication Engineering, K. Ramakrishnan College of Engineering, Tiruchirappalli 621 112, India

4 Department of Chemistry, Vinayaka Mission's Kirupananda Variyar Arts and Science College, Vinayaka Missions Research Foundation (DU), Salem, India

Published online: 24 October 2025

[12–14]. However, its low conductivity limits performance, necessitating integration with conductive materials.

Combining $MnNi_2S_4$ and MOF-67 leverages their pseudocapacitive and structural advantages. These composites improve charge distribution, enhance ion diffusion, and increase specific surface area, resulting in superior specific capacitance and cycling stability compared to individual components [15–17]. This synergistic strategy addresses conductivity and mechanical limitations, promoting next-generation energy storage systems.

GO features high surface area, oxygen-functional groups, and excellent dispersibility, aiding the uniform distribution of active materials in supercapacitors. While GO alone offers limited conductivity, it enhances charge transport in hybrid structures [16].

The rGO, obtained via chemical or thermal reduction of GO, partially restores graphene's structure, significantly enhancing conductivity. Its residual functional groups improve interaction with metal oxides and sulfides. rGO-based composites exhibit enhanced performance due to their conductivity, surface area, and mechanical strength. When integrated with $MnNi_2S_4$ and MOF-67, rGO creates a stable, high-performance structure combining pseudocapacitance, porosity, and conductivity [18]. The hydrothermal method has emerged as a widely used and versatile technique for synthesizing nanostructured materials due to its ability to control particle size, morphology, and crystallinity. This method enables the formation of highly crystalline products at relatively low temperatures and pressures, and it is particularly effective for producing oxide-based materials with well-defined structures. Additionally, the hydrothermal process allows for the uniform doping of heteroatoms and the integration of composite phases, making it suitable for designing multifunctional materials. However, the technique also presents certain limitations, such as longer reaction durations, the requirement of high-pressure vessels (autoclaves), and limited scalability in certain industrial settings. Despite these drawbacks, its advantages in terms of material quality and structural control make it a preferred method in many electrochemical and energy storage applications. Hydrothermal Synthesis of $NiMn_2S_4$ involves dissolving Nickel and Manganese chlorides with thiourea in water, using a 1:2 Ni: Mn ratio. After stirring and optional pH adjustment, the mixture is sealed in a Teflon-lined autoclave and heated (160–200 °C, 10–24 h). The black $NiMn_2S_4$ precipitate is collected, washed, and dried. This method enables controlled morphology and high surface area. Characterization via XRD, SEM, and CV confirms structural and electrochemical properties [19, 20].

The roadmap for $MnNi_2S_4$-MOF-ZIF-67@rGO includes six stages: (1) Material Design—selecting $MnNi_2S_4$ and ZIF-67 for their redox activity and porosity, and rGO for conductivity; (2) Synthesis Optimization—a two-step hydrothermal process optimizing temperature/time for nanostructure stability; (3) Characterization—XRD, SEM, TEM, and elemental mapping to verify morphology and distribution; (4) Electrochemical Testing—CV and impedance spectroscopy to evaluate capacitance and cycling stability; (5) Performance Scaling—adjusting ratios for scalability; and (6) Prototype Testing—assembling into devices and testing under real conditions. This approach aims to produce a high-performance, scalable, and commercially viable supercapacitor electrode.

2 Experimental section

2.1 Materials and methods

Graphite Powder, Potassium Permanganate ($KMnO_4$), Sodium Nitrate ($NaNO_3$), Sulfuric Acid (H_2SO_4), Hydrochloric Acid (HCl), Hydrogen Peroxide (H_2O_2), Graphene Oxide, a reducing agent (such as hydrazine hydrate), 2-methylimidazole, Methanol, Cobalt (II) Nitrate Hexahydrate ($Mn(NO_3)_2$•6 H_2O), Nickel(II) chloride hexahydrate ($NiCl_2$·6 H_2O), Manganese chloride hexahydrate ($MnCl_2$·6 H_2O) and Thiourea were obtained from Merck India.

2.2 Synthesis of $NiMn_2S_4$ and MOF-ZIF-67

The hydrothermal synthesis of $NiMn_2S_4$ is a precise method for creating nanostructured materials with controlled particle size and morphology. The process begins with an aqueous solution of Nickel chloride ($NiCl_2$•6 H_2O) and Manganese chloride ($MnCl_2$•6 H_2O) in a 1:2 molar ratio, mixed with excess thiourea as a sulfur source. The pH can be adjusted if needed, and the solution is stirred thoroughly before being transferred to a Teflon-lined autoclave. Heated at 160–200 °C for 10–24 h, this reaction produces a black $NiMn_2S_4$ precipitate. After cooling, the precipitate is washed and dried to yield $NiMn_2S_4$ powder.

MOF-ZIF-67 is synthesized via a solvothermal method using Cobalt (II) Nitrate hexahydrate ($Co(NO_3)_2$•6 H_2O) and 2-methylimidazole in a methanol and DMF solvent mixture. The solution is transferred to a Teflon-lined autoclave, sealed, and heated to 120 °C for 24 h to facilitate crystal growth. The pH of the solution was maintained 11 using ammonia solution. After cooling, the product is washed with methanol to remove impurities and dried at 60 °C for 12 h to obtain MOF-ZIF-67 powder. Both synthesis procedures, as shown in Fig. 1, yield materials with optimized structural and electrochemical properties.

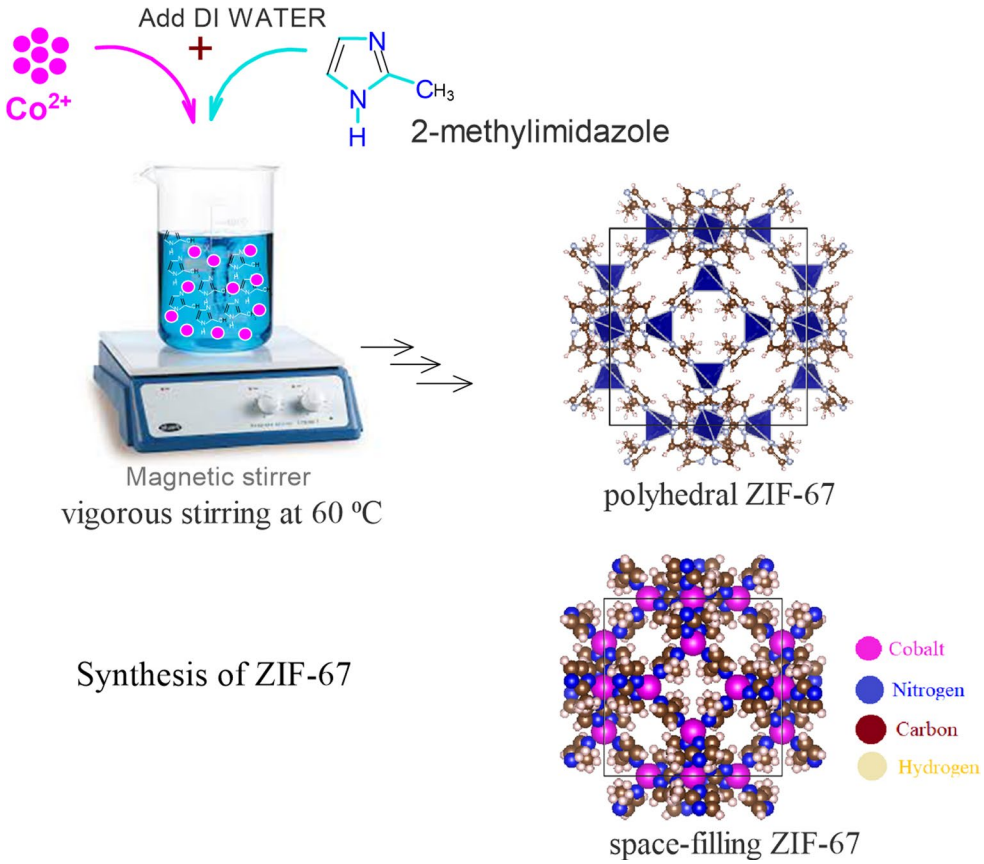

Fig. 1 The proposed synthesis process of the ZIF-67 material

2.3 Synthesis of reduced graphene oxide (rGO) and $NiMn_2S_4$-MOF-ZIF-67@rGO nanocomposite

The synthesis of reduced graphene oxide (rGO) involves reducing graphene oxide (GO) with hydrazine hydrate. First, GO is dispersed in deionized water to create a stable suspension, to which hydrazine hydrate is added dropwise while stirring continuously. The mixture is then heated to 90 °C and maintained for 24 h to ensure full reduction. After cooling, the rGO is washed with deionized water and ethanol to remove any residual reactants and is finally dried at 60 °C for 12 h, resulting in purified rGO.

The synthesis of $NiMn_2S_4$-MOF-ZIF-67@rGO nanocomposite involves combining $NiMn_2S_4$, MOF-ZIF-67, and rGO in deionized water, followed by 30 min of sonication to achieve a well-dispersed mixture, as depicted in Fig. 2. This mixture is then transferred to a Teflon-lined stainless-steel autoclave and heated at 120 °C for 12 h to facilitate interaction and formation of the nanocomposite. Once cooled to room temperature, the product is washed with deionized water and ethanol, then dried at 60 °C for 12 h. This hydrothermal synthesis method integrates $NiMn_2S_4$, ZIF-67, and rGO into a functional composite, enhancing its properties for advanced applications in energy storage, electrocatalysis, and sensing.

2.4 Supercapacitor electrode fabrication method

Supercapacitors store and deliver energy rapidly due to their asymmetric electrode-electrolyte configuration. The fabrication process uses carbon-based materials like reduced graphene oxide (rGO) for their high surface area and conductivity. Binders such as polyvinylidene fluoride (PVDF) or polytetrafluoroethylene (PTFE) ensure adhesion and stability. Reduced graphene oxide (rGO), obtained via chemical reduction of GO, was used to enhance electrical conductivity and facilitate electron transport, overcoming the intrinsic low conductivity of GO. N-methyl-2-pyrrolidone (NMP) acts as a solvent to create a uniform slurry, and aluminum foil or stainless-steel serves as the electrode substrate.

A magnetic stirrer and ultrasonic bath help mix and disperse the materials evenly. The slurry is then applied to the substrate with a doctor blade or spin coater, achieving a consistent coating. After drying in an oven to remove solvent residues, the electrode is compressed with a hot press or roll press for optimal adhesion and thickness. This method

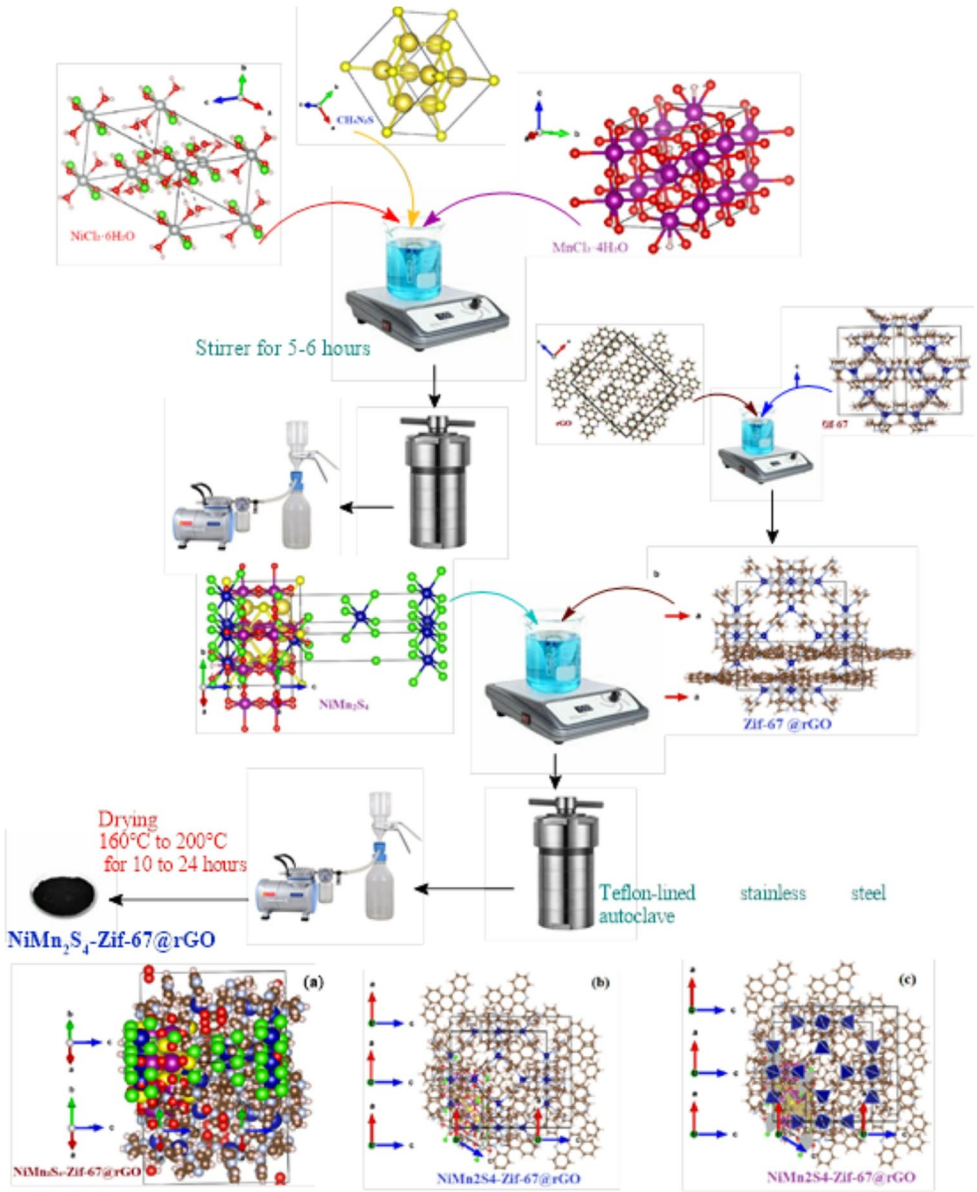

Fig. 2 Depicts a systematic procedure for the hydrothermal synthesis of a $NiMn_2S_4$-Zif-67@rGOnanocomposite. **a** Nanocrystallographic Space filling Structure, **b** Nanocrystallographic Stick-and-Ball Structure and **c** Nanocrystallographic polyhedral Structure

produces high-quality anode and cathode electrodes, making them ready for integration into supercapacitors for effective energy storage and delivery.

2.5 Procedure for supercapacitor electrode fabrication and assembly

2.5.1 Preparation of electrode slurry

To prepare the anode slurry, combine 10 wt% graphene oxide powder, 80 wt% $NiMn_2S_4$-MOF-ZIF-67@rGO nanocomposite, 10 wt% polytetrafluoroethylene (PTFE) binder, and N-methyl-2-pyrrolidone (NMP) solvent. For the cathode, mix 10 wt% graphene oxide powder, 10 wt% PTFE, and NMP solvent. Disperse the carbon material in the solvent using a magnetic stirrer for 30 min, then sonicate for an additional 30 min to achieve a homogeneous suspension. Finally, add the binder and conductive additive, stirring for 2 h to form a uniform electrode slurry.

2.5.2 Fabrication of anode and cathode electrodes

Cut the substrate (aluminum foil or stainless steel) to the required size and shape, then apply the slurry using a doctor blade or spin coater, adjusting the thickness as needed. Place the coated substrate in a drying oven at 80 °C for several hours to remove any remaining solvent and create a solid electrode layer.

2.5.3 Assembly of the supercapacitor

Position a separator (e.g., cellulose paper or polymeric membrane) between the anode and cathode to prevent direct contact. Immerse the electrodes in a 1 M KOH electrolyte solution for several hours, allowing the electrolyte to saturate the porous layers. Seal the assembled supercapacitor in appropriate packaging to prevent electrolyte leakage, ensuring stability and durability for long-term use.

2.6 Fabrication of $NiMn_2S_4$-MOF-ZIF-67@rGO//GO asymmetric supercapacitor (ASC) devices

2.6.1 Preparation of electrode materials

For the ASC device, the $NiMn_2S_4$-MOF-ZIF-67@rGO composite is used as the positive electrode, while graphene oxide (GO) serves as the negative electrode. *Assembly of ASC Devices*: The ASC is assembled by placing a separator, such as filter paper, between the positive and negative electrodes. The separator is soaked in a 1 M KOH electrolyte solution to ensure ionic conductivity, and copper wires are used to connect the electrodes and complete the circuit. *Electrochemical Characterization*: The ASC device's electrochemical performance is evaluated using cyclic voltammetry (CV) to assess charge-storage capacity and energy efficiency, galvanostatic charge-discharge (GCD) testing to measure energy density and power density, and electrochemical impedance spectroscopy (EIS) to analyze internal resistance and stability. These characterization techniques collectively determine the ASC's effectiveness for high-performance energy storage applications.

2.7 Characterization methods of supercapacitors

FTIR identifies functional groups and bonding interactions within supercapacitor materials, providing insights into the chemical structure, composition, and any synthesis modifications impacting performance. XRD determines crystalline structure and phase purity, giving information on crystal grain arrangement and size, which affects conductivity and stability in energy storage. SEM images the surface morphology and microstructure, revealing particle shape, size, and porosity, all essential for ion storage and fast charge/discharge capacity.

CV assesses charge-storage mechanisms and capacity, offering data on the reversibility, stability, and energy efficiency of electrochemical reactions. GCD testing evaluates energy density, power density, and efficiency, providing insights into cycle stability and device lifespan. EIS measures internal resistance and charge-transfer properties, helping assess impedance, ion diffusion, and suitability for high-power applications. Together, these methods provide a comprehensive assessment of a supercapacitor's properties, guiding the optimization for enhanced energy storage and performance.

3 Results and discussion

3.1 FTIR and Raman spectral analysis

The FTIR analysis reveals the structural and chemical properties of each material, confirming the integration of components in the $NiMn_2S_4$-MOF ZIF-67@rGO composite, as shown in Fig. 3.

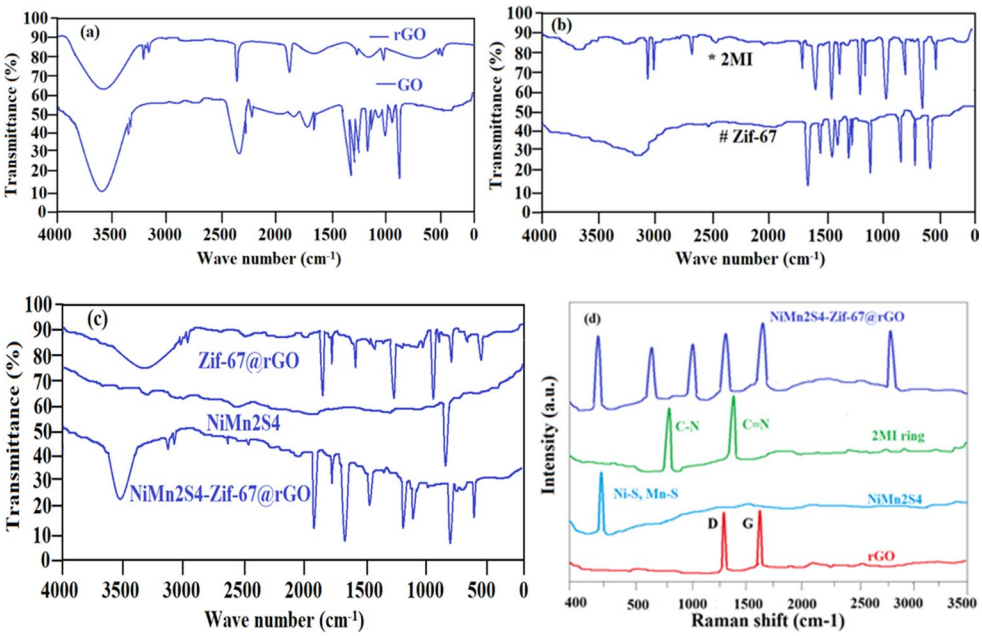

Fig. 3 FTIR Spectra of (**a**) GO, rGO, (**b**) *2MI and # Zif-67,(**c**) Zif-67@rGO, NiMn2S4 and $NiMn_2S_4$-MOF ZIF-67@rGO and (**d**) Raman spectrum

Graphite shows weak peaks in the FTIR spectrum due to its non-polar, crystalline structure with minimal functional groups. Minor peaks may indicate trace impurities or slight oxidation. *Graphene Oxide (GO)* displays prominent peaks from oxygen-containing functional groups, such as a broad O–H stretch around 3300–3400 cm^{-1}, C = O stretching at 1720 cm^{-1}, C = C skeletal vibrations at 1620 cm^{-1}, and C–O stretching in epoxy groups around 1050 cm^{-1} [21]. These peaks confirm the oxidation of graphite to GO, adding functional groups that enhance GO's reactivity. *Reduced Graphene Oxide (rGO)* shows significantly reduced oxygen-functional group peaks, reflecting partial reduction [Fig. 3d]. A small O–H peak around 3400 cm^{-1} and diminished C = O and C–O peaks indicate the removal of oxygen, while a strong C = C peak at 1620 cm^{-1} confirms the restored sp^2 carbon structure. *MOF ZIF-67* exhibits characteristic imidazole ligand peaks, with C–H stretching at 3130 cm^{-1} and 2920 cm^{-1}, C = N stretching at 1580 cm^{-1}, and bands for C–N and N–H bending around 1140 cm^{-1} and 690 cm^{-1}, confirming the ZIF-67 framework's formation. *MOF ZIF-67@rGO* combines ZIF-67 and rGO features, with the ZIF-67 peaks, such as C = N stretching at 1580 cm^{-1}, still visible. The C = C peak near 1620 cm^{-1} from rGO confirms the integration of rGO with ZIF-67, while a slight reduction in the O–H peak suggests interaction between rGO and the ZIF-67 framework, potentially improving conductivity. *$NiMn_2S_4$* shows metal-sulfur (M–S) bonds with characteristic Ni–S and Mn–S stretching peaks below 600 cm^{-1}, confirming the formation of the $NiMn_2S_4$ structure. *$NiMn_2S_4$-MOF ZIF-67@rGO* combines features from all components, confirming successful integration. Peaks from ZIF-67, such as C = N stretching at 1580 cm^{-1}, remain, along with reduced GO bands around 1620 cm^{-1} for C = C. New peaks below 600 cm^{-1} indicate Ni–S and Mn–S bonds, confirming the presence of $NiMn_2S_4$ in the composite. The FTIR spectrum suggests the formation of a functional hybrid material with properties ideal for energy storage applications.

3.2 X-ray diffraction (XRD) analysis of Graphite, GO, rGO, MOF ZIF-67, MOF ZIF-67@rGO, $NiMn_2S_4$, and $NiMn_2S_4$-MOF ZIF-67@rGO

The XRD analysis provides critical information on the crystalline structures and integration of each material component within the $NiMn_2S_4$-MOF ZIF-67@rGO nanocomposite, as shown in Fig. 4. *Graphite* shows a sharp peak at $2\theta \approx 26.5°$, corresponding to the (002) plane, indicating a well-ordered, crystalline structure with minimal defects. *Graphene Oxide (GO)* exhibits a broad peak around 10–12° (001 plane), reflecting intercalation of oxygen-containing groups and increased interlayer spacing due to oxidation, leading to a more amorphous structure. *Reduced Graphene Oxide (rGO)* shows a peak shift toward 24–25° (between graphite and GO peaks), signifying partial reduction with restored graphitic structure and some remaining defects. *MOF ZIF-67* displays distinct peaks at 7.3°, 10.4°, and 12.7°, which correspond to the crystal planes of the ZIF-67 framework, confirming its highly ordered structure. *MOF ZIF-67@rGO* combines both ZIF-67 and rGO peaks, indicating successful integration. ZIF-67 peaks remain visible, while a broader rGO peak around 24–25° appears, enhancing the composite's conductivity and surface area.*$NiMn_2S_4$* exhibits characteristic peaks at 30°, 35°, and 53°, confirming a cubic or tetragonal metal sulfide structure [1, 14].

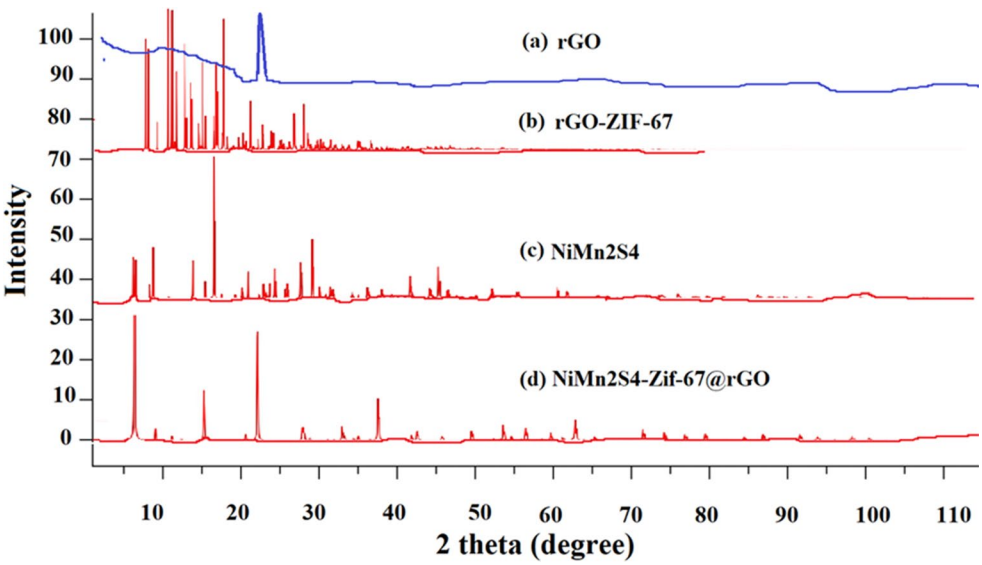

Fig. 4 X-ray Diffraction (XRD) Patterns of rGO, ZIF-67@rGO, $NiMn_2S_4$, and $NiMn_2S_4$- ZIF-67@rGO

The high crystallinity of $NiMn_2S_4$ supports its role as an active material in energy storage. *$NiMn_2S_4$-MOF ZIF-67@rGO* shows a combination of peaks from ZIF-67 (e.g., 7.3°, 10.4°, and 12.7°), $NiMn_2S_4$ (30°, 35°, and 53°), and rGO (24–25°), confirming successful integration of all components. Peaks at 32.12° and 26.34° indicate Ni-Mn-S presence and Ni foam stability within the structure, respectively. The XRD patterns and peak intensities, matching closely with JCPDS card 020–0782, validate the cubic crystal structure of $NiMn_2S_4$-MOF ZIF-67@rGO, with lattice parameters $a=b=c=16.90770$ Å, angles $\alpha=\beta=\gamma=90°$, and unit-cell volume of 4833.4092 $Å^3$. This structural arrangement enhances conductivity, stability, and suitability of the composite for energy storage applications.

3.3 Raman spectroscopy analysis of $NiMn_2S_4$-MOF ZIF-67@rGO

Raman spectroscopy is a key technique for analyzing the molecular structure and composition of the $NiMn_2S_4$-MOF ZIF-67@rGO nanocomposite, confirming the successful integration of $NiMn_2S_4$, ZIF-67, and rGO within the composite as shown in Fig. 3(d). *rGO Bands*: The Raman spectrum of rGO shows two prominent peaks: the D-band around 1350 cm^{-1}, which indicates disordered carbon structures, and the G-band near 1580 cm^{-1}, representing graphitic sp^2-hybridized carbon. The moderate ID/IG ratio suggests partial reduction of graphene oxide, enhancing the composite's conductivity. *$NiMn_2S_4$ Vibrations*: Peaks in the 250–500 cm^{-1} range correspond to Ni–S and Mn–S bond vibrations, confirming the presence of metal sulfide in the composite. These peaks indicate strong metal-sulfur bonding, which is essential for the redox activity contributing to high specific capacitance [15, 22].

ZIF-67 Framework Peaks: The ZIF-67 component is identified by peaks at 680 cm^{-1} and 1450 cm^{-1}, related to C–N and C=N stretching vibrations within the imidazole ring. These peaks confirm the structural stability of the MOF even after integration with rGO and $NiMn_2S_4$, contributing to the composite's high surface area and active sites for redox reactions. Synergistic Interactions: The combined Raman spectrum confirms the successful integration of all components, with slight shifts in peak positions due to interactions between $NiMn_2S_4$, ZIF-67, and rGO. These interactions enhance electron transfer pathways, improving conductivity, stability, and specific capacitance. Raman spectroscopy provides structural insights that support the electrochemical performance of $NiMn_2S_4$-MOF ZIF-67@rGO, confirming its potential as a high-performance electrode material for supercapacitors and advanced energy storage applications.

3.4 Scanning electron microscopy (SEM) analysis of graphite, GO, rGO, MOF ZIF-67, MOF ZIF-67@rGO, $NiMn_2S_4$, and $NiMn_2S_4$-MOF ZIF-67@rGO

SEM analysis provides insights into the morphology of each material and confirms the successful integration of components in the $NiMn_2S_4$-MOF ZIF-67@rGO composite as shown in Fig. 5. *Graphite*: Shows a layered, flaky morphology with compactly stacked smooth surfaces, characteristic of its crystalline structure, but with limited surface area and porosity. *Graphene Oxide (GO)*: Displays a wrinkled and rough surface with separated layers due to oxygen-containing groups, creating a porous network that enhances surface area and provides sites for ion adsorption. *Reduced Graphene Oxide (rGO)*: SEM images reveal partially restored stacked layers with reduced wrinkles and moderate porosity, offering improved conductivity and structural integrity. **MOF** *ZIF-67*: Exhibits a polyhedral morphology, with rhombic dodecahedron-shaped crystals and uniform size distribution. This well-defined shape contributes to high surface area for catalytic and adsorption applications. *MOF ZIF-67@rGO*: SEM shows ZIF-67 particles anchored on rGO sheets, with ZIF-67 crystals enhancing surface area and rGO providing a conductive support matrix, promoting efficient electron transfer. *$NiMn_2S_4$*: Features a porous, flower-like nanoflake structure that increases surface area and facilitates electrolyte contact, beneficial for ion transport and capacitive performance in energy storage.

SEM reveals a complex, hierarchical structure with $NiMn_2S_4$ nanoflakes and ZIF-67 particles uniformly distributed on rGO sheets. This architecture enhances surface area, promotes ion transport, and optimizes electron transfer and stability, ideal for high-performance supercapacitors. The SEM analysis confirms the successful integration of each material in the composite, with a morphology that maximizes surface area, conductivity, and structural stability for effective energy storage applications.

3.5 X-ray photoelectron spectroscopy (XPS) analysis of $NiMn_2S_4$-ZIF-67@rGO

XPS analysis of the $NiMn_2S_4$-ZIF-67@rGO composite reveals the chemical composition and oxidation states of key elements, including Ni, Mn, S, C, N, and O, which contribute to the composite's electrochemical properties, as shown in Fig. 6. *Nickel (Ni)*: The Ni 2p spectrum shows peaks around 855 eV and 873 eV, corresponding to Ni^{2+}, confirming Ni's role in redox reactions within the supercapacitor, where it acts as an active site for faradaic charge storage. *Manganese (Mn)*: The Mn 2p spectrum exhibits peaks at 641 eV and 653 eV, indicating the presence of Mn^{2+}

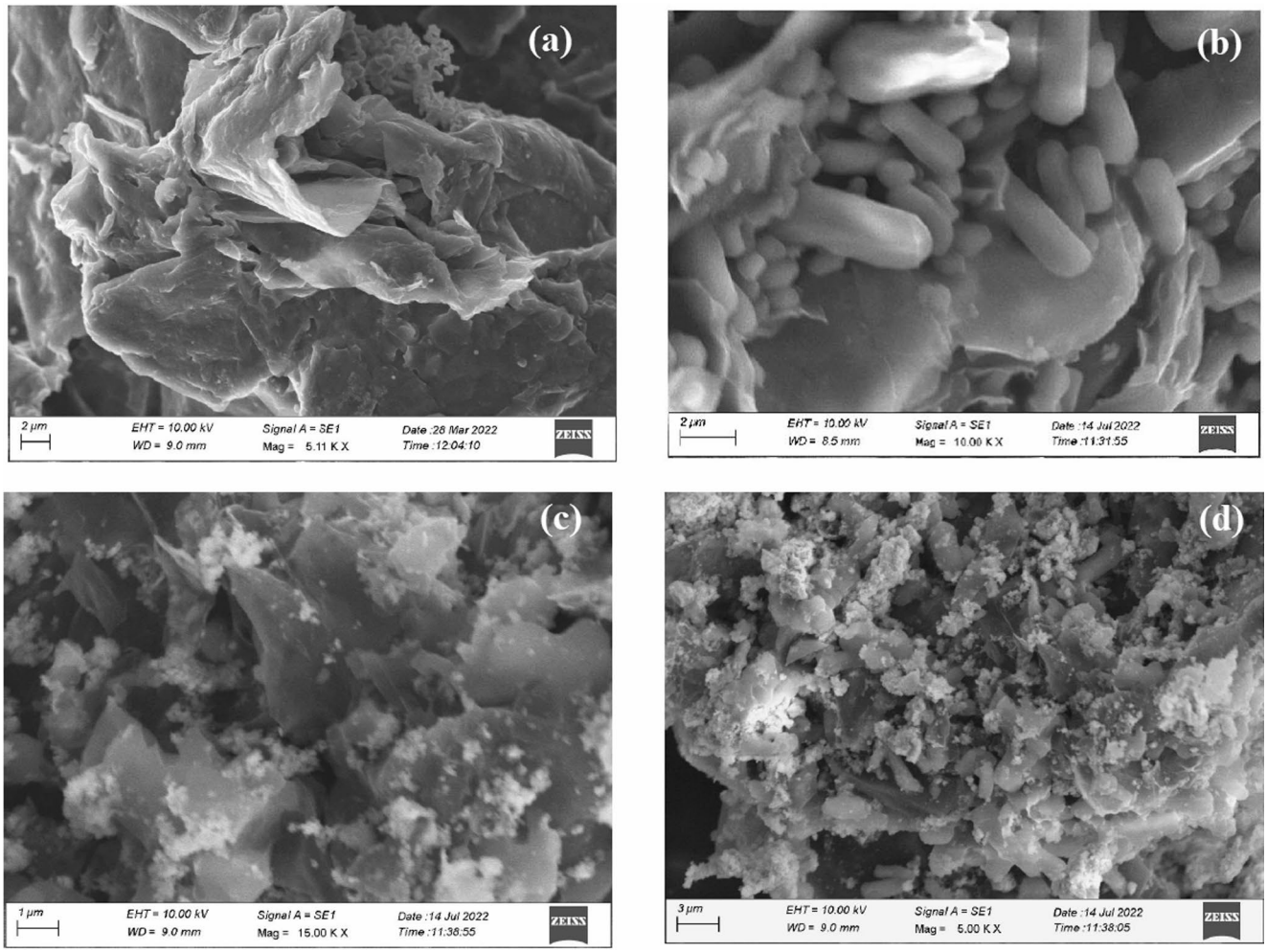

Fig. 5 Depicts low- and high-resolution scanning electron microscope (SEM) images of various materials: **a** reduced graphene oxide (rGO), **b** ZIF-67/rGO composite, and **c** NiMn2S4 and **d** NiMn2S4-Zif-67@rGO composite

and Mn^{3+} oxidation states. This coexistence enhances the pseudocapacitance of the composite, as Mn participates in reversible redox reactions, supporting high specific capacitance. *Sulfur (S)*: The S 2p spectrum shows a peak at 162 eV, corresponding to S^{2-} in $NiMn_2S_4$, stabilizing Ni and Mn ions in the composite and balancing charge transfer for enhanced redox activity and stability. *Carbon (C)*: The C 1 s spectrum displays peaks at 284.8 eV, 286 eV, and 288 eV, corresponding to C–C/C = C, C–O, and O–C = O bonds. These indicate graphitic carbon from rGO and oxygen-containing groups, contributing to electrical conductivity and improved electron transport. *Nitrogen (N)*: The N 1 s spectrum shows a peak at 399 eV, associated with nitrogen in the ZIF-67 framework (C = N bond in the imidazole ring), enhancing surface area and providing active sites for ion adsorption. *Oxygen (O)*: The O 1 s spectrum shows peaks at 531 eV and 533 eV, linked to metal-oxygen bonds (Ni–O, Mn–O) and C–O bonds from rGO. These bonds enhance stability, supporting electrode integrity and additional ion adsorption for improved capacitance. XPS analysis confirms the presence and integration of each element in the composite, highlighting the synergistic roles of Ni, Mn, S, and rGO, with ZIF-67 contributing additional active sites, making $NiMn_2S_4$-ZIF-67@rGO a promising material for high-performance supercapacitors [5, 6, 14].

3.6 Electrochemical studies of $NiMn_2S_4$-ZIF-67@rGO//GO

3.6.1 Cyclic voltammetry (CV) and specific capacitance analysis of $NiMn_2S_4$-ZIF-67@rGO//GO

The cyclic voltammetry (CV) analysis of the $NiMn_2S_4$-ZIF-67@rGO//GO composite demonstrates its suitability as a supercapacitor electrode material, as shown in Fig. 7. The CV curves exhibit prominent redox peaks due to faradaic reactions of Ni and Mn ions in the $NiMn_2S_4$ structure, indicating pseudocapacitive behavior that enables

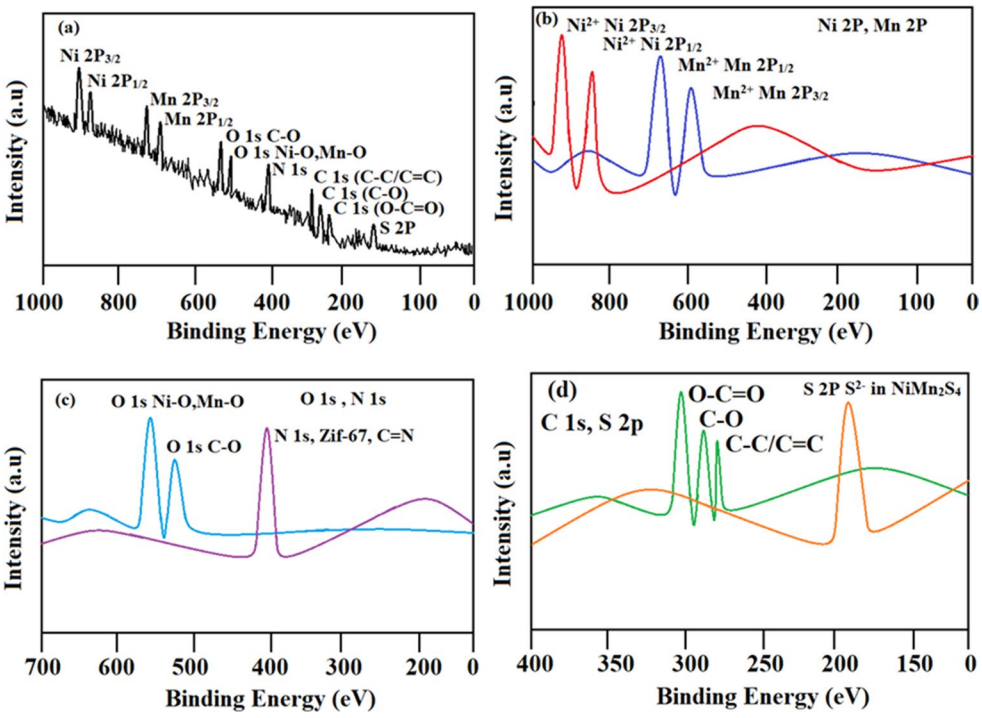

Fig. 6 The X-ray photoelectron spectroscopy (XPS) analysis of the $NiMn_2S_4$-Zif-67@rGO composite material is depicted. The figure includes the following spectra: **a** XPS survey spectrum, **b** Ni 2p and Mn 2p, **c** O1s and N1s, and **d** S2p

high specific capacitance through reversible redox reactions beyond electric double-layer capacitance. The composite's CV curves maintain stable redox peak positions across different scan rates, with minimal distortion, showcasing excellent rate capability and suitability for high-power applications. This stability suggests efficient ion and electron transport, supported by rGO's conductive network and the high surface area of ZIF-67, which facilitates ion diffusion.

Specific capacitance (Cs) values were calculated from the CV curves using the Eq. 1 [23–25].

$$Cs = \frac{1}{mv\,(Vc - Va)} \int_{Va}^{Vc} I\,(V)\,dV \tag{1}$$

Where:

- Cs is the specific capacitance (F g^{-1}),
- m is the mass of the electrode,
- V_c–V_a is the potential window,
- v is the scan rate, and.
- I (V) represent the current as a function of voltage.

where Cs values were found to be 1550 F g^{-1}, 1330 F g^{-1}, 1150 F g^{-1}, 1030 F g^{-1}, and 990 F g^{-1} at scan rates of 10 mV/s, 20 mV/s, 30 mV/s, 40 mV/s, and 100 mV/s, respectively. This decrease in capacitance with increasing scan rate is typical for pseudocapacitive materials, as higher scan rates limit ion diffusion and reduce electrode utilization. These results confirm that $NiMn_2S_4$-ZIF-67@rGO//GO retains high specific capacitance even at elevated scan rates, highlighting its potential for high-performance supercapacitor applications. The composite's excellent rate capability makes it well-suited for applications that require both high power density and stable performance across various operational conditions.

3.6.2 Specific capacitance analysis and interpretation of galvanostatic Charge-Discharge (GCD) for $NiMn_2S_4$-ZIF-67@rGO//GO

The specific capacitance ($C_{specific}$) of $NiMn_2S_4$-ZIF-67@rGO//GO was calculated using Eq. 2:

$$C_{specific} = \frac{I \times \Delta t}{m \times \Delta V} \tag{2}$$

Where,

I is the applied current density,

Δt is the discharge time,

m is the mass of the active material, and.

ΔV is the potential window.

The GCD curves for $NiMn_2S_4$-ZIF-67@rGO//GO show a smooth slope without distinct plateaus, suggesting a hybrid energy storage mechanism where both electric double-layer

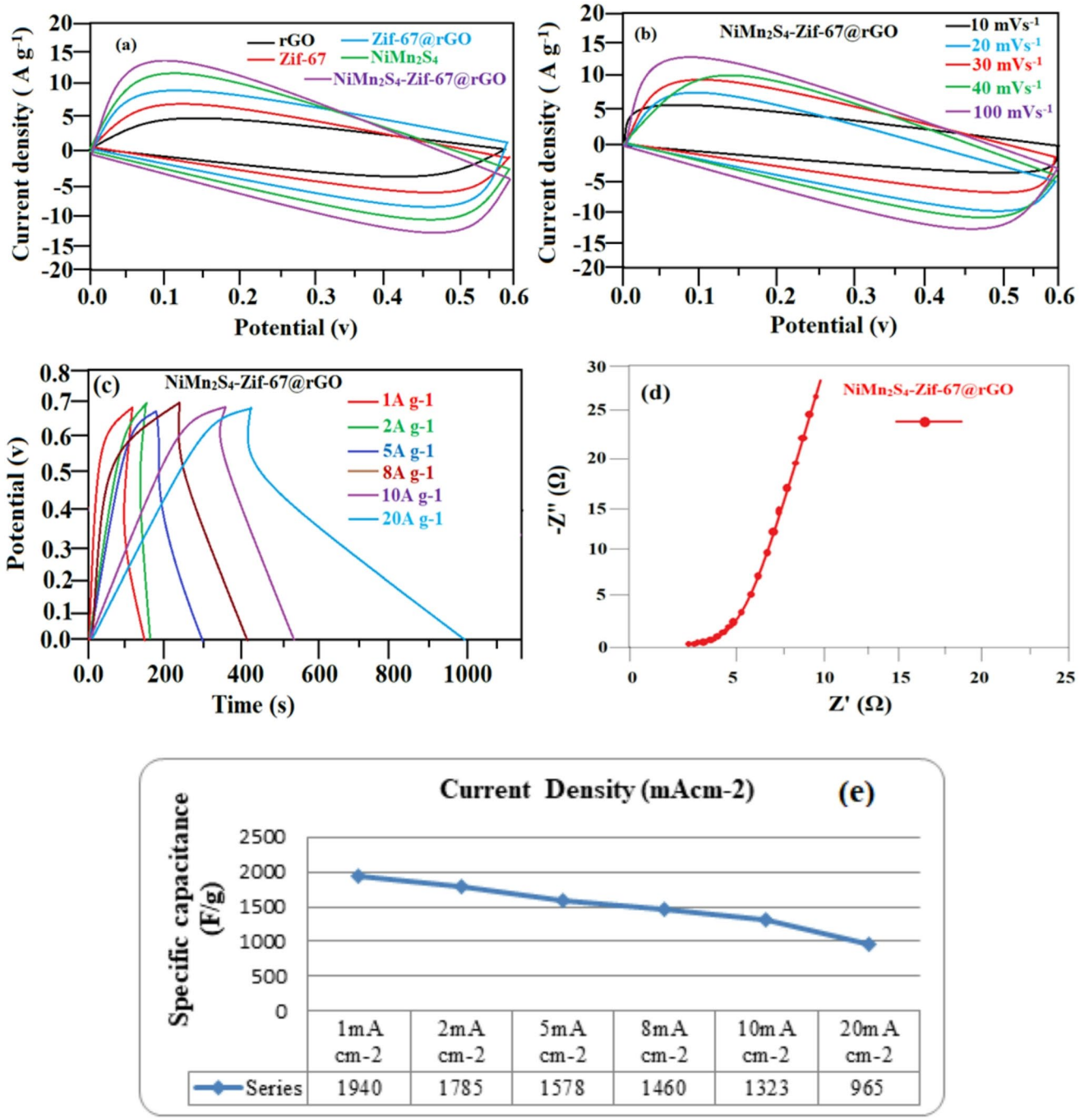

Fig. 7 **a**: CV curves of rGO, ZIF-67,ZIF-67@rGO, $NiMn_2S_4$ and $NiMn_2S_4$-Zif-67@rGO//GO at 10 mV/s. **b** $NiMn_2S_4$-Zif-67@rGO// GO at various scan rates. **c**: GCD curves of $NiMn_2S_4$-Zif-67@rGO// GO at various specific currents. **d**: Nyquist plots of $NiMn_2S_4$-Zif-67@ rGO//GO. **e** Specific capacity versus specific current

capacitance (EDLC) and pseudocapacitance contribute. The EDLC is provided by the high surface area of rGO, while pseudocapacitance arises from the redox reactions of Ni and Mn ions in the $NiMn_2S_4$ structure. The specific capacitance values for $NiMn_2S_4$-ZIF-67@rGO//GO were recorded at various current densities in a 6 M KOH electrolyte, yielding values of 1940, 1785, 1578, 1460, 1323, and 965 F g^{-1} for current densities of 1, 2, 5, 8, 10, and 20 A g^{-1}, respectively. The decrease in capacitance with increasing current density is typical for supercapacitors, as higher current densities limit ion diffusion and reduce active material utilization. The rate performance showed strong specific capacitance retention even at increased current densities. The composite also achieved a specific energy (Es) of 45.90 Wh kg^{-1} at a

specific power (Ps) of 1689 W kg^{-1} using Eqs. 3 and 4, making it well-suited for high-power applications.

Additionally, the $NiMn_2S_4$-ZIF-67@rGO//GO composite demonstrated excellent cycling stability, retaining 82% of its initial capacitance after 3000 charge-discharge cycles. This stability results from rGO's conductive network and structural support, along with active redox sites provided by ZIF-67 and $NiMn_2S_4$. The combination of high specific capacitance, strong rate performance, and durability positions $NiMn_2S_4$-ZIF-67@rGO//GO as a promising electrode material for advanced supercapacitors.

To calculate energy density (E) in Watt-hours per kilogram (Wh kg^{-1}) and power density (P) in Watts per kilogram (W kg^{-1}) using specific capacitance (C) in Farads per gram (F g^{-1}), the correct formulas are as follows [16, 26]:

$$Energy\ Density:\ E = \frac{1}{2} \times C \times V^2 \tag{3}$$

$$Power\ Density:\ P = \frac{E}{t \times 3600} \tag{4}$$

where: E: energy density (in Watt-hours per kilogram, Wh kg^{-1}) C: specific capacitance (in Farads per gram, F g^{-1}) V: operating voltage (in volts) t: discharge time (in seconds).

3.6.3 Electrochemical impedance spectroscopy (EIS) analysis of $NiMn_2S_4$ ZIF67@rGO//GO

EIS analysis was conducted to examine the electrical properties of the $NiMn_2S_4$-ZIF-67@rGO//GO composite, synthesized with an equimolar Ni/Mn ratio. The Nyquist plot, illustrated in Fig. 7(d), reveals key aspects of charge transfer and ion diffusion within the composite.

Nyquist plot analysis The plot displays a characteristic semicircular arc in the high-frequency region, indicating charge transfer resistance (Rct) at the electrode-electrolyte interface, and a linear tail in the low-frequency region, corresponding to Warburg impedance (Zw), associated with ion diffusion. This dual profile indicates that the composite undergoes both charge transfer and diffusion-controlled processes, essential for high-performance supercapacitors [27].

Electrochemical impedance The impedance magnitude (|Z|) and phase angle (θ) were measured across a frequency range. A lower |Z| at high frequencies signifies efficient charge transfer, beneficial for high-power applications. *Charge Transfer Resistance* ***(Rct)*** is derived from the semicircle's diameter in the high-frequency region of the Nyquist plot. A relatively low Rct indicates efficient electron transfer, attributed to the conductive rGO network and the high surface area of ZIF-67, which support rapid charge transfer and reduced resistance. *Double Layer Capacitance* ***(Cdl)*** is calculated from the linear portion of the Nyquist plot in the low-frequency region. This value reflects the composite's surface area and charge storage capability at the electrode-electrolyte interface. A higher Cdl suggests increased surface area and enhanced ion adsorption, suitable for supercapacitor applications. *Warburg Impedance* ***(Zw)***: The linear tail at lower frequencies corresponds to Zw , indicating ion diffusion within the electrode material. The interconnected rGO pathways and porous ZIF-67 structure facilitate ion transport, which is critical for stability during extended charge-discharge cycles. *Impedance Values Summary*: The $NiMn_2S_4$-ZIF-67@rGO//GO composite shows low Rct (around 1.3 Ω) and high Cdl (approximately 25 F g^{-1}), along with favorable Zw for ion diffusion. This combination of properties supports the composite's ability to deliver both high power density and excellent cycling stability. The EIS analysis demonstrates that $NiMn_2S_4$-ZIF-67@rGO//GO exhibits superior electrochemical performance with fast charge transfer and efficient ion transport. These characteristics make it a highly promising material for supercapacitors, capable of providing robust performance, high power density, and stable cycling for advanced energy storage applications.

The calculated the exact values for impedance magnitude (|Z|), phase angle (θ), charge transfer resistance (Rct), double layer capacitance (Cdl), Warburg impedance (Zw), and solution resistance (Rs) of $NiMn_2S_4$-ZIF-67@rGO//GO, detailed EIS data points and Nyquist plot values would be needed, typically obtained from experimental EIS measurements, calculated values would be organized in a table format if the data were available (Table 1 and Table 2):

4 Conclusion

The hydrothermal synthesis of the $NiMn_2S_4$-ZIF-67@rGO//GO electrode material has demonstrated remarkable enhancements in key performance metrics, making it a strong contender for energy storage applications. The composite achieved an impressive specific capacitance of 1940 F g^{-1} at 1 A g^{-1}, highlighting its superior charge storage capability. Furthermore, it exhibited a high power density of 1689 W kg^{-1}, ensuring rapid energy delivery, while maintaining a substantial energy density of 45.90 Wh kg^{-1} at the same power level, confirming its excellent energy storage potential. The electrode also showcased outstanding cycling stability, retaining 88.2% of its initial capacitance after 5000 cycles at 5 A g^{-1}, emphasizing its durability and long-term operational reliability. These results underscore the

Table 1 Calculated parameter from Nyquist plot analysis

Parameter	Symbol	Calculated Value	Units	Description
Impedance Magnitude	(|Z|)	22.36	Ohms (Ω)	Nyquist plot data that shows the real and imaginary parts of impedance, Z′ (real part) and Z‴ (imaginary part), across different frequencies.
Phase Angle	θ	68.2∘	Degrees	Angle between applied voltage and resulting current, reflecting capacitive or resistive behavior.
Charge Transfer Resistance	Rct	1 Ω	Ohms (Ω)	Resistance associated with charge transfer at the electrode-electrolyte interface.
Double Layer Capacitance	Cdl	64 F	Farads (F)	Capacitance of the electric double layer at the interface, indicating surface area and charge storage.
Warburg Impedance	Zw	0.63–0.63j Ω	Ohms (Ω)	Reflects ion diffusion within the electrode material; lower values indicate efficient ion transport.
Solution Resistance	Rs	2.5 Ω	Ohms (Ω)	Resistance due to the electrolyte solution and cell components.

Table 2 Comparative specific capacitance of NiMn2S4-Zif-67@rGO//GO ASC cell and other earlier reports

S. No.	Positive Electrode	Negative Electrode	Current density	Electrolyte	Operational Voltage	Specific capacitance (F g^{-1})	Ref.
1	$NiCo_2S_4$@Mo-doped Co-LDH	Activated carbon (AC)	1 A g^{-1}.	3 M KOH	0-0.6	3049.3 F g^{-1}	[22]
2	ZIF-67/$CoNi_2S_4$	Yolk-Shell carbon spheres (YS-CS)	4 A g^{-1}	1MKOH	0-0.4	1890 F g^{-1}	[23]
3	Ni-Co-S/G	Activated carbon (AC)	1 A g^{-1}	1MKOH	0-0.7	1579.68 F g^{-1}	[24]
4	$NiCo_2S_4$@PPy	Activated carbon (AC)	1 A g^{-1}	1MKOH	0–1.0	1842.8 F g^{-1}	[25]
5	ZIF-67/rGO	ZIF-67/rGO	4.5 A g^{-1}	0.2 M $K_3[Fe(CN)_6]$ in 1 M Na_2SO_4	−0.1 to 0.5	1453 F g^{-1}	[26]
6	ZIF-9 derived rGO/$NiCo_2S_4$	Activated carbon (AC)	1 A g^{-1}	1MKOH	0-0.5	1242.2 F g^{-1}	[16]
7	rGO-10/$NiCo_2S_4$ derived from ZIF-67	Activated carbon (AC)	1 A g^{-1}	3MKOH	0-0.5	171 mAh g^{-1}	[27]
8	ZIF-67/rGO/NiPc	Activated carbon (AC)	1 A g^{-1}	1MKOH	0-0.5	860 F g^{-1}	[28]
9	Co–Ni LDH	Activated carbon (AC)	2.0 A g^{-1}	3MKOH	0-0.6	1232 F g^{-1}	[29]
10	ZIF-67/$NiCo_2S_4$	CoS_2	1 A g^{-1}	2 M KOH	0-1.4	287 C g^{-1}	[30]
11	ZIF-67/NiCoS/ Carbon Cloth (CC)	Activated carbon (AC)	0.5 A g^{-1}	2 M KOH	0-1.5	128 F g^{-1}	[31]
12	ZIF-67/CC/CNWAs@Ni@Co-Ni2S4	Activated carbon (AC)	1 A g^{-1}	1 M KOH	0-1.6	151.3 F g^{-1}	[32]
13	ZIF-67/NiCo2S4@C	Activated carbon (AC)	1 A g^{-1}	1 M KOH	0-1.6	948.9 F g^{-1}	[33]
14	**NiMn2S4-Zif-67@rGO**	GO	1 A cm^{-2}	6 MKOH	0-1.7	1940 F g^{-1}	[34]

effectiveness of integrating ZIF-67 and rGO in enhancing electrochemical performance by increasing conductivity, active sites, and structural stability. The successful synthesis of this high-performance composite electrode highlights the immense potential of MOF-derived transition metal sulfide materials for next-generation energy storage devices, paving the way for further advancements in high-power and high-energy-density applications.

Acknowledgements A.S would like to express gratitude to the Principal and DST-FIST sponsored ACIC, St. Joseph's College (Autonomous), Tiruchirappalli-620 002, for providing essential infrastructure facilities. Additionally, P.K. extends thanks to Prof. K.Priyadarshini, Department of ECE, K. Ramakrishnan College of Engineering, Tiruchirappalli, for her invaluable support and encouragement in research activities. Furthermore, Researcher Dr. C.M. sincerely acknowledges all members of the Dr. C. Mani LABS team for their cooperative and kind assistance.

Author contributions **S. Antony Sakthi** conceived the idea and designed the study. **K. Priyadarshini** conducted the statistical analysis, contributed to manuscript preparation, and provided critical feedback. **C.Mani** and **A. Niresha Gnana Mary** performed the experiments and analyzed the data, and offered technical assistance and contributed to data interpretation. **E. Shinyjoy** done the English correction and Editing. All authors reviewed and approved the final manuscript for submission.

Data availability The authors confirm that the data supporting the findings of this study are available within the article.

Declarations

Conflict of interest The authors affirm that there are no conflicts of interest associated with this research. The funding sources did not influence the study's design, data acquisition, analysis, interpretation, manuscript preparation, or the decision to submit it for publication. Furthermore, there are no financial affiliations with any entities that could have affected the design or interpretation of the study's outcomes.

References

1. D.C. Marcano, D.V. Kosynkin, J.M. Berlin, ACS Nano. **4**, 4806–4814 (2010). https://doi.org/10.1021/nn1006368
2. C. Gao, Z. Dong, X. Hao et al., ACS Omega. **5**, 9903–9911 (2020). https://doi.org/10.1021/acsomega.0c00183
3. A.M. Dimiev, J.M. Tour, ACS Nano. **8**, 3060–3068 (2014). https://doi.org/10.1021/nn500606a
4. D. Chen, H. Feng, J. Li, Chem. Rev. **112**, 6027–6053 (2012). https://doi.org/10.1021/cr300115g
5. F. Li, X. Jiang, J. Zhao, S. Zhang, Nano Energy. **16**, 488–515 (2015). https://doi.org/10.1016/j.nanoen.2015.07.014
6. S.N. Alam, N. Sharma, L. Kumar, Graphene. **6**, 1–18 (2017). https://doi.org/10.4236/graphene.2017.61001
7. J. Jagiełło, A. Chlanda, M. Baran et al., Nanomaterials (Basel). **10**, 1846 (2020). https://doi.org/10.3390/nano10091846
8. do J.R. Nascimento, M.R. D'Oliveira, A.G. Veiga et al., ACS Omega. **5**, 25568–25581 (2020). https://doi.org/10.1021/acsomega.0c02417
9. L. Stobinski, A. Lesiak, A. Malolepszy et al., J. Electron. Spectrosc. Relat. Phenom. **195**, 145–154 (2014). https://doi.org/10.1016/j.elspec.2014.07.003
10. N.R. Wilson, A. Priyanka, R. Beanland et al., ACS Nano. **3**, 2547–2556 (2009). https://doi.org/10.1021/nn900694t
11. N. Cao, Y. Zhang, *J. Nanomater.* **2015**, 5 (2015). https://doi.org/10.1155/2015/168125
12. C. Wang, F. Yu, K. Lu et al., Ind. Eng. Chem. Res. **61**, 7952–7961 (2022). https://doi.org/10.1021/acs.iecr.2c00685
13. Y. Guo, J. Tang, H. Qian et al., Chem. Mater. **29**, 5566–5573 (2017). https://doi.org/10.1021/acs.chemmater.7b00867
14. R. Zhu, J. Ding, J. Yang et al., ACS Appl. Mater. Interfaces. **12**, 25037–25041 (2020). https://doi.org/10.1021/acsami.0c05450
15. X. Chen, D. Liu, G. Cao et al., ACS Appl. Mater. Interfaces. **11**, 9374–9384 (2019). https://doi.org/10.1021/acsami.8b22478
16. S. Sundriyal, V. Shrivastav, H. Kaur et al., ACS Omega. **3**, 17348–17358 (2018). https://doi.org/10.1021/acsomega.8b02065
17. M. Zhao, A.T. Reda, D. Zhang, ACS Omega. **5**, 8012–8022 (2020). https://doi.org/10.1021/acsomega.0c00089
18. M. Shahsavari, M. Mortazavi, S. Tajik et al., Micromachines. **13**, 88 (2022). https://doi.org/10.3390/mi13010088
19. C. Siyi Kang, J. Wang, T. Chen, E. Meng, Jiaqiang, J. Energy Storage. **67**, 107515 (2023). https://doi.org/10.1016/j.est.2023.107515
20. M.Z.U. Abidin, M. Ikram, S. Moeen, G. Nazir, M.B. Kanoun, Souraya Goumri-Said. Coord. Chem. Rev. **520**, 216158 (2024). https://doi.org/10.1016/j.ccr.2024.216158
21. X. Feng, Q. Jiao, H. Cui et al., ACS Appl. Mater. Interfaces. **10**, 29521–29531 (2018). https://doi.org/10.1021/acsami.8b08547
22. D. Yuan, G. Huang, D. Yin et al., ACS Appl. Mater. Interfaces. **9**, 18178–18186 (2017). https://doi.org/10.1021/acsami.7b02176
23. S. Cheng, K. Du, X. Wang et al., Nanomaterials. **13**, 2663 (2023). https://doi.org/10.3390/nano13192663
24. Q. Wang, F. Gao, B. Xu et al., Chem. Eng. J. **327**, 387–396 (2017). https://doi.org/10.1016/j.cej.2017.06.124
25. Y. Jin, A. Sun, J. Geng et al., Diam. Relat. Mater. **137**, 110151 (2023). https://doi.org/10.1016/j.diamond.2023.110151
26. J. Li, Y. Zou, B. Li et al., Ceram. Int. **47**, 16562–16569 (2021). https://doi.org/10.1016/j.ceramint.2021.02.227
27. Y. Cui, L. Zhao, H. Pan et al., Microchem J. **190**, 108718 (2023). https://doi.org/10.1016/j.microc.2023.108718
28. S. Wu, X. Xu, X. Sun, S. Zhou, C. Liu, P. Zhang, S. Fu, H. Zhang, S. Pang, X. Wang, Q. Yang, Diam. Relat. Mater. **136**, 109946 (2023). https://doi.org/10.1016/j.diamond.2023.109946
29. J. Mu, Z. Guo, Y. Zhao et al., J. Mater. Sci. Mater. Electron. **33**, 17733–17744 (2022). https://doi.org/10.1007/s10854-022-08636-5
30. G. Liu, H. Zhang, J. Li et al., J. Mater. Sci. **54**, 9666–9678 (2019). https://doi.org/10.1007/s10853-019-03536-2
31. D. Guo, X. Song, L. Tan, H. Ma, H. Pang, X. Wang, L. Zhang, ACS Appl. Mater. Interfaces. **10**(49), 42621–42629 (2018). https://doi.org/10.1021/acsami.8b14839
32. T. Liu, J. Liu, L. Zhang, B. Cheng, J. Yu, J. Mater. Sci. Technol. **47**, 113–121 (2020). https://doi.org/10.1016/j.jmst.2019.12.027
33. Y. Wang, J. Huang, Y. Xiao, Z. Peng, K. Yuan, L. Tan, Y. Chen, Carbon. **147**, 146–153 (2019). https://doi.org/10.1016/j.carbon.2019.02.082
34. W. Cao, Y. Liu, F. Xu, Q. Xia, G. Du, Z. Fan, N. Chen, Electrochim. Acta. **385**, 138433 (2021). https://doi.org/10.1016/j.electacta.2021.138433